processes

MDPI

Article

Hyperbolic Evolutionary Model for Equivalent Modulus of Sand and Characterization of Its Cyclic Hardening Properties

Xueqing Wu [1], Longtan Shao [1,*], Xiaojian Tian [2] and Pingxin Xia [3]

[1] Department of Engineering Mechanics, Dalian University of Technology, Dalian 116000, China
[2] State Key Laboratory of Intelligent Mining Equipment Technology, Taiyuan Heavy Industry Co., Ltd., Taiyuan 030024, China
[3] School of Urban Construction, Changzhou University, Changzhou 213164, China
* Correspondence: shaolt2022@163.com

Abstract: The cyclic hardening characteristics of soil hold significant importance for understanding its performance, and the evolution of the deformation modulus serves as a crucial indicator of the hardening properties. Deformations can be classified into elastic and plastic deformations and expressed in terms of modulus; however, their roles in the cyclic hardening process remain unclear. In this study, the elastic and plastic moduli were separated using the hyperbolic evolutionary model, which characterized the evolutionary properties of both to reflect the cyclic hardening process. A series of cyclic triaxial shear tests was conducted utilizing ISO sand and emery as test materials. A hyperbolic evolution model relating the equivalent modulus to the number of cycles was established, and the effect of various test conditions on the elastic modulus is discussed. The results indicate that: (1) the relationship between the equivalent modulus and the number of cycles is hyperbolic; and (2) the parameters k and b of the hyperbolic evolution model correspond to the elastic and plastic moduli, allowing for the separation of the evolution of both from that of the deformation modulus. The hyperbolic evolution model of the equivalent modulus proposed in this paper offers new insight into the cyclic hardening properties of sand.

Keywords: equivalent modulus; hyperbolic evolution model; elastoplastic separation; cyclic triaxial test

Citation: Wu, X.; Shao, L.; Tian, X.; Xia, P. Hyperbolic Evolutionary Model for Equivalent Modulus of Sand and Characterization of Its Cyclic Hardening Properties. *Processes* **2024**, *12*, 2550. https://doi.org/10.3390/pr12112550

Academic Editor: Antoni Sanchez

Received: 23 October 2024
Revised: 12 November 2024
Accepted: 13 November 2024
Published: 14 November 2024

1. Introduction

Cyclic loads represent a common type of loading, such as traffic loads, which act on transportation infrastructure, and wave loads, which act on piles [1,2]. The cyclic loading imposed on a structure is transferred to the soil through the foundation, resulting in soil strength degradation and fatigue, thereby compromising the safety and life cycle of the structure [3–5]. Granular material (soil) demonstrates a gradual hardening behavior under cyclic loading, primarily manifested in the increasing steepness of the stress–strain hysteresis loop; that is, the deformation modulus progressively increases with the number of cycles [6–8]. Consequently, understanding the cyclic hardening behavior of soil and quantifying evolution of the deformation modulus are essential for safeguarding the service performance of geotechnical structures.

Several studies have been conducted on the evolutionary behavior of the deformation modulus of soil under cyclic loading, and various elastic–plastic theoretical models have been established [9–12]. A common feature among them is that elastic strain occurs within a small strain range inside the yield surface, whereby cyclic loading within this region produces only elastic strain. Indeed, the deformation of soil represents elastic–plastic coupling behavior, and taking the elastic–plastic coupling effect into account enhances the predictive capability of the soil constitutive model [13,14]. The total deformation modulus of the soil comprises the coupling of the elastic and plastic moduli, which can be partially decoupled into the elastic modulus E^{elastic} and the plastic modulus E^{plastic} [15]. Neglecting plastic

deformation within the yield surface and assuming that only elastic deformation occurs inside it may compromise the accuracy of subsequent plasticity parameter measurements. Hence, to more realistically depict the cyclic hardening behavior of sand, attention should be directed towards the evolution of the elastic and plastic moduli throughout the cyclic process following the decoupling of the total deformation modulus.

At present, the evolutionary behavior of the soil elastic modulus under stress cycling remains unclear. For the sake of convenience, Pradhan and Tatsuoka [16] assumed that elasticity remains constant under cyclic loading; however, this assumption lacks a theoretical basis and experimental evidence. Karg and Haegeman [17] conducted cyclic triaxial tests and observed that the elastic properties of the soil remained nearly constant during cyclic loading within a narrow strain range. Nonetheless, most of these conclusions emphasize the elastic detection of soil in a narrow strain range. In reality, the relatively large stress increments generated in granular material during unloading can surpass the transient elastic limit of soil [18,19], failing to fully characterize the continuous elastic behavior of the soil. Zeng and Shao [6] proposed a novel method for determining the elastic modulus of soils over a large strain range, which was further validated by Xia et al. [8,20]. They pointed out that the elastic response of sand in a stable state under cyclic loading can serve as an evaluation of the true elastic properties of granular soil in cyclic unloading triaxial tests with large stress amplitudes. Nevertheless, the data exhibit considerable volatility in response to changes in elastic properties due to stress history, and do not provide definitive conclusions.

Regarding the evolution of the plastic modulus, there are relatively fewer studies based on experimental data, and most begin from plasticity theory. To describe the hysteretic response of soil in cyclic loading, various plasticity assumptions such as yield function, plastic potential surface, and hardening theory have been introduced to accommodate the loading–unloading process by continuously adjusting the state of the yield surface. One of the most widely used theories is the multiple yield surface plasticity theory [21,22], upon which numerous models have been developed. For instance, Mroz and Norris [23,24] established a multi-yield surface model that captures the softening phenomenon of soil, and the current relative position of the yield surface is used to reflect the change of the plastic modulus. However, specific criteria for determining this parameter are not provided, and the multiple yield surface model is computationally complex, limiting its practical application. To solve this issue, Dafalias et al. [10] simplified the model to a double-yield-surface approach, retaining only two yield surfaces, one functioning as the bounding surface and the other as the loading surface, with each surface governed by its own independent equations. However, in practice, there are instances where the model-predicted axial strain accumulation exceeds the actual measured value [25]. Subsequently, Dafalias et al. [26] established a bounding surface model by compressing the loading surface to a point based on the two-sided model, which further simplified the model. Due to its significant simplification in mathematical operations, it has been extensively applied in practical engineering. Nonetheless, the evolution of the plastic modulus continues to be derived through assumptions. In summary, this type of theory often requires the establishment of formulas for the calculation of the plastic modulus by means of the dimensions and positions of the yield and boundary surfaces, the evolution of which is pre-assumed and simplified. Therefore, the determination of model parameters often requires assumptions through the trial-and-error method, and the effectiveness in reflecting the evolution of the real plastic behavior of the soil body needs to be improved.

An analysis of the potential cyclic evolutionary behavior of plasticity based on the generalized plasticity theory also exists [27]: its most important feature is that the model does not directly specify the yield surface or the plastic potential surface, but rather provides a formula for the plastic modulus. Pastor [28] applied the generalized plasticity theory to describe the stress–strain behavior of sand and clay under cyclic loading. To explain the cyclic hysteresis phenomenon more accurately, he introduced a discrete memory factor to adjust the plastic modulus. Heidarzadeh and Oliaei [29] proposed a novel approach to

defining the generalized plastic modulus applicable to sand through the introduction of bounding surface theory. Though in the generalized plasticity theory, the plastic modulus is directly calculated using a mathematical formula, which simplifies the modeling process, it also introduces challenges such as numerous parameters and unclear physical significance. Moreover, the formula for the plastic modulus is also based on pre-assumptions, and the plastic modulus is likely to deviate from the true value in engineering applications.

To address the shortcomings of the above studies, this paper defines the equivalent modulus from the experimental point of view from the evolution of the total deformation modulus to reflect the cyclic hardening process. Utilizing a full-surface deformation digital image measurement system, a series of large-stress-amplitude triaxial cyclic loading tests was conducted on ISO sand and emery. The stress–strain behavior of sand during cyclic triaxial tests and the evolution of the equivalent modulus with respect to the number of cycles are analyzed. Additionally, a hyperbolic model relating the equivalent modulus to the number of cycles is established, and the physical significance of two key parameters in the model is examined. The model not only provides an accurate description of the equivalent modulus during the test but also separates the elastic and plastic components of the cyclic process. Moreover, the model does not necessitate the introduction of plastic assumptions, such as plastic potential surface or hardening law, thereby offering new insights into the evolution of the deformation modulus of sandy soil under cyclic loading with large stress amplitudes.

2. Materials and Methods

The test platform consists of a triaxial testing machine equipped with a full-surface-deformation digital image measurement system (DIMS) developed by Shao et al. [30,31], as shown in Figure 1. The error of the axial and radial strain of DIMS was 10^{-5}. Unlike the white latex rubber membrane used in traditional triaxial tests, the platform uses a black latex rubber membrane with 8 rows and 8 columns of 7 mm × 7 mm white squares uniformly distributed on the outer surface, as shown in Figure 2. The dorsal image of the rubber membrane is captured by the camera after being reflected off the left- and right-plane mirrors, resulting in a total of 240 recognizable effective corner points in Figure 2b. The corner points of each white square serve as feature points for image measurement and recognition, and are identified and tracked using a sub-pixel corner recognition algorithm. A CMOS camera captures the deformation process of the specimen, monitors its surface displacement in real time by identifying characteristic points on the rubber membrane's surface in the image, and calculates the surface deformation based on geometric equations and isoparametric transformations using the finite element method.

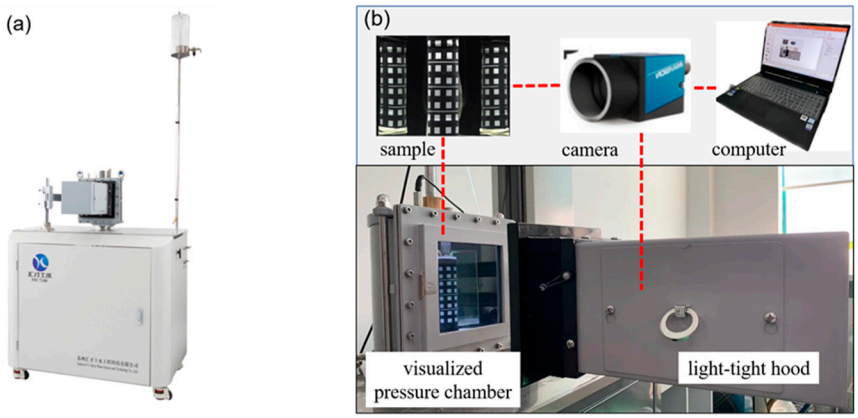

Figure 1. Composition of the whole-surface-deformation measurement system: (**a**) triaxial apparatus; (**b**) digital image measurement system.

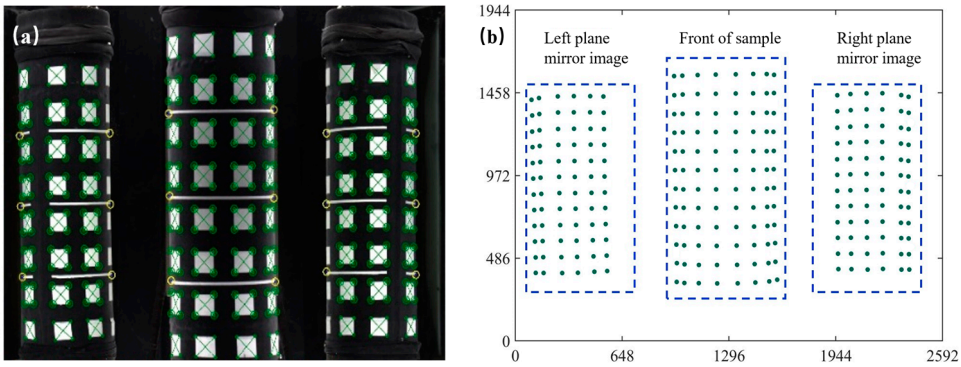

Figure 2. (**a**) Corner identification of the sample; (**b**) pixel coordinates of corner points (unit: pixel).

The test materials consisted of ISO sand (SS) and emery (ES). Their grading curves are shown in Figure 3. The materials were dried and formed into standard cylindrical specimens with diameter Φ = 39.1 mm and height H = 80 mm. The constant loading and unloading rate was set to 0.1 mm/min. The time history of deviatoric stress and stress path are shown in Figure 4. Table 1 lists the test program.

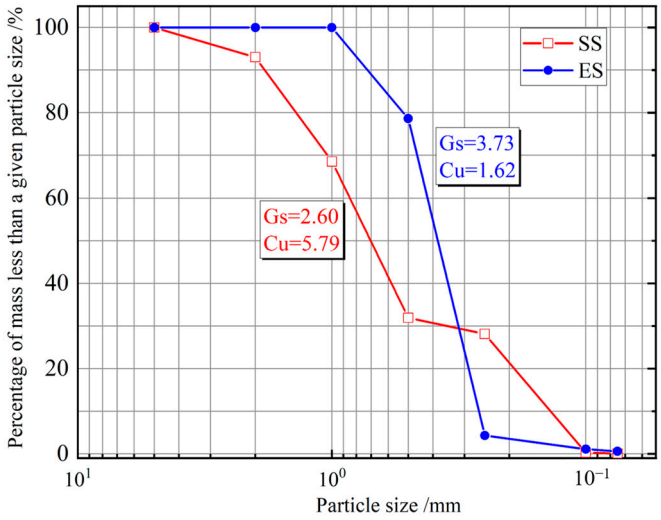

Figure 3. Physical indices of experiment material.

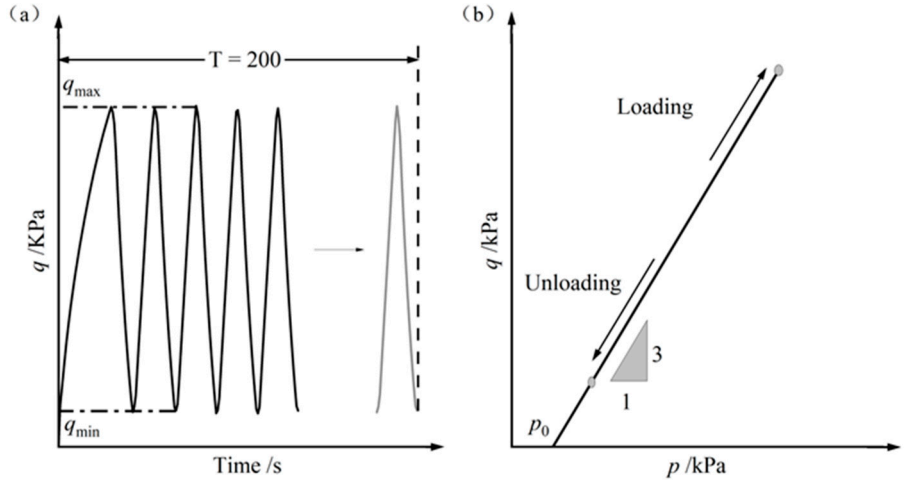

Figure 4. (**a**) Deviatoric stress versus time; (**b**) stress path in *p*–*q* space.

Table 1. Program of triaxial loading–unloading testing.

Test Number	Dry Density ρ_d g/cm^3	Relative Density D_r %	Initial Void Ratio e_0 -	Confining Pressure σ_3 kPa	Maximum Deviator Stress q_{max} kPa
SSC121	1.682	30	0.546	200	300
SSC211	1.754	50	0.482	100	300
SSC221	1.754	50	0.482	200	300
SSC222	1.754	50	0.482	200	400
SSC223	1.754	50	0.482	200	500
SSC231	1.754	50	0.482	300	300
SSC251	1.754	50	0.482	400	300
SSC321	1.792	60	0.451	200	300
SSC421	1.874	80	0.387	200	300
ESC121	1.836	30	1.032	200	300
ESC211	1.898	50	0.965	100	300
ESC221	1.898	50	0.965	200	300
ESC222	1.898	50	0.965	200	400
ESC223	1.898	50	0.965	200	500
ESC231	1.898	50	0.965	300	300
ESC251	1.898	50	0.965	400	300
ESC321	1.931	60	0.932	200	300
ESC421	2.000	80	0.865	200	300

3. Results

The typical stress–strain curves of the specimens in the cyclic triaxial tests are shown in Figure 5. The results indicated that axial strain increased with the number of cycles, though the growth rate diminished, as evidenced by a gradual and densely packed distribution of the curves. The results also revealed that the specimen underwent substantial strain during the first cycle, contrasting sharply with the minor strain increments in subsequent cycles. This indicates that the deformation characteristics of the specimen in the first cycle differed from those in the other cyclic phases, aligning with the analyses of Xiong [32], Tong [33], and Buckovalas [34] et al. For instance, consider tests SSC223 and ESC223. The relationship between axial strain and time is illustrated in Figure 6, indicating that as the test proceeds, axial strain increases during loading, decreases during unloading, and results in plastic cumulative strain at the end of each cycle. Moreover, as the test progresses, the axial strain continues to increase, but its growth curve becomes increasingly flat. A comparison of stress–strain curves for different cycles is shown in Figure 7. The shape of the stress–strain curve of the cycle changes significantly, with the cycle interval decreasing until a stable and unchanging hysteresis loop emerges. The cyclic loading stress–strain curve nearly returns to the origin after reaching the steady state, suggesting that no further irrecoverable strain occurs within the cycle.

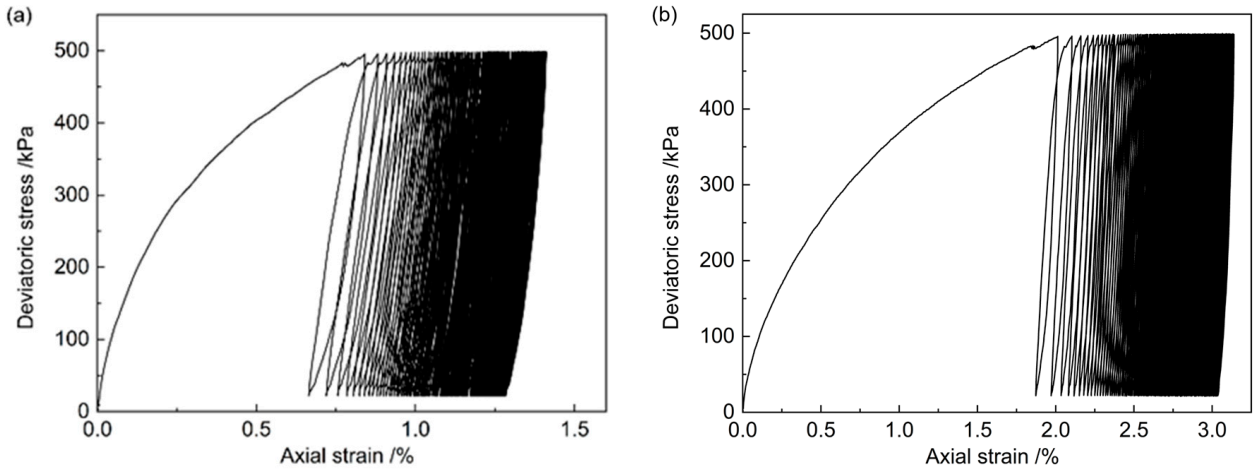

Figure 5. Overall stress–strain curve: (**a**) SSC223; (**b**) ESC223.

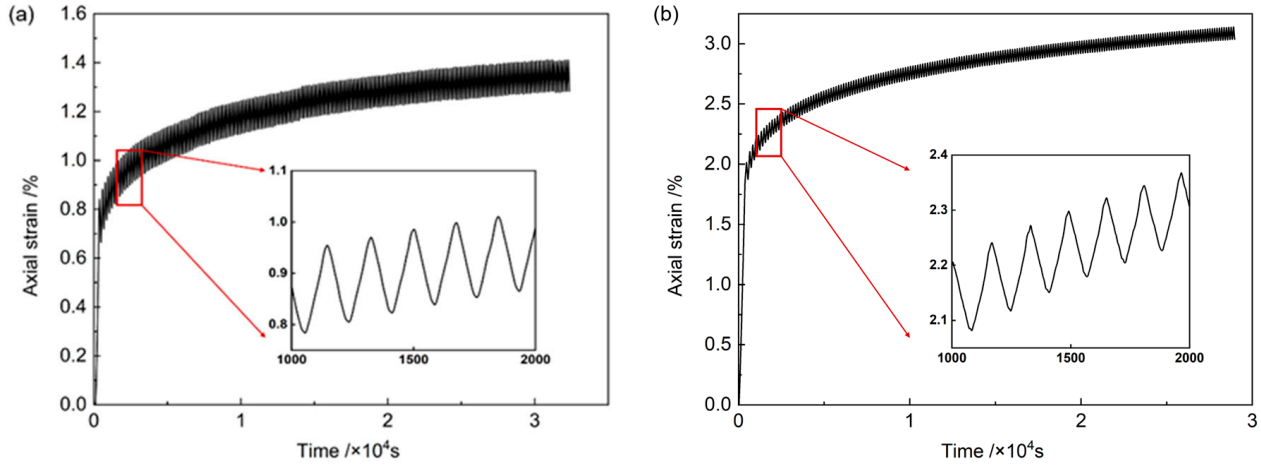

Figure 6. Change in axial strain: (**a**) SSC223; (**b**) ESC223.

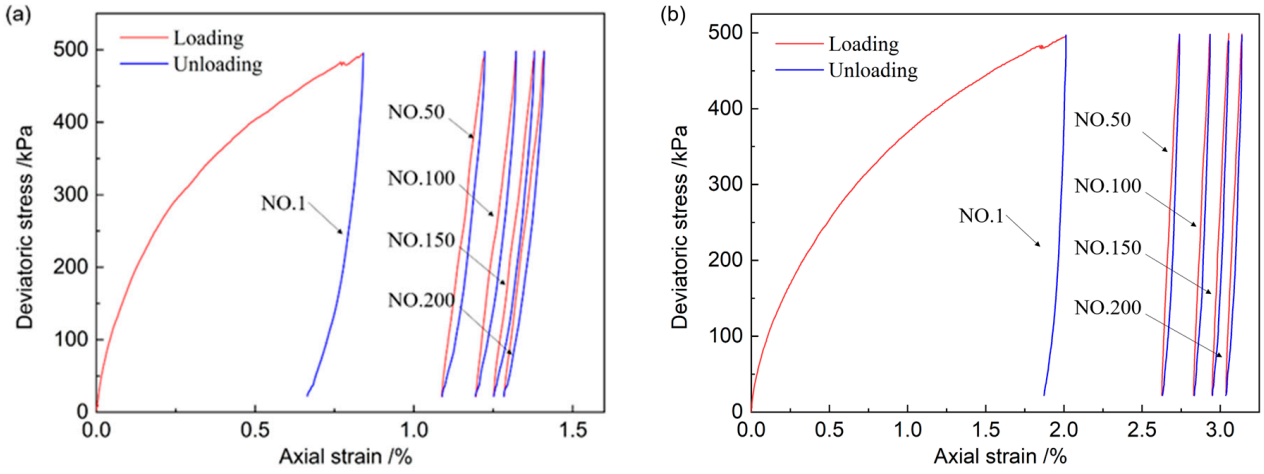

Figure 7. Stress–strain curves for different cycles: (**a**) SSC223; (**b**) ESC223.

4. Discussion

4.1. Hyperbolic Law Between Equivalent Modulus and Number of Cycles

Drawing from the stress–strain curves obtained from the triaxial cyclic loading and unloading tests, the equivalent modulus was introduced to quantify the deformation characteristics of the loading and unloading phases within each cycle. The ratio of the deviatoric stress increment to the corresponding axial strain increment during the loading and unloading phases was defined as the loading and unloading equivalent modulus in the cycle, as shown in Equation (1) and Figure 8:

$$E^N = \frac{\Delta q}{\Delta \varepsilon} \tag{1}$$

where E^{N} is the loading (or unloading) equivalent modulus in the Nth cycle; Δq is the deviatoric stress increment within the loading (or unloading) stage in the Nth cycle; and $\Delta \varepsilon$ is the axial strain increment within the corresponding stage. In Figure 8, E^1_{load} and E^1_{unload} are the secant moduli for the first loading and the first unloading, respectively. Point A is the end of the loading phase, and point B is the end of the unloading phase.

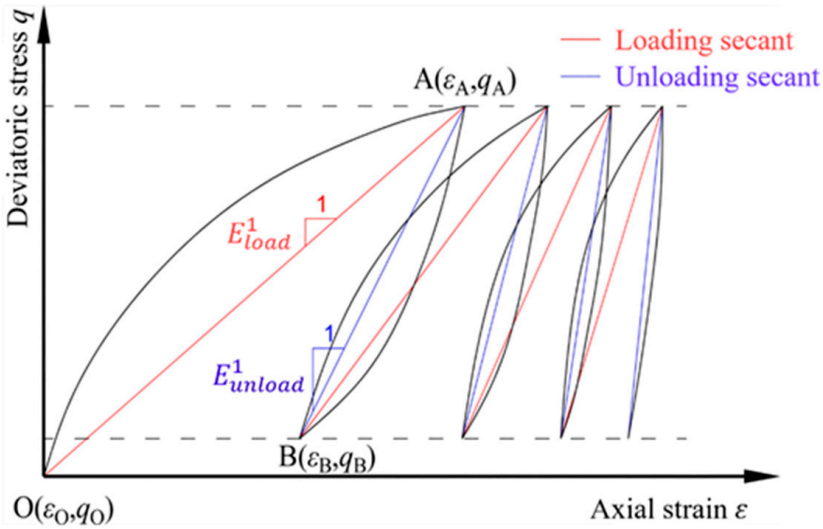

Figure 8. Definition of equivalent moduli at the loading and unloading stage.

In the constant-amplitude cyclic loading and unloading tests, the increment in axial strain in each cycle diminished with an increasing number of cycles, as evidenced by the continuous rise in the equivalent modulus during loading and unloading. Using test SSC223 as an example for analysis, Figure 9 shows that the loading equivalent modulus at the onset of the test was considerably smaller than the unloading equivalent modulus for the same cycle, as evidenced by the rapid accumulation of axial strain. However, the unloading equivalent modulus always fluctuated within a narrow range. This is because the deformation caused by loading is significantly greater than the rebound deformation caused by unloading in the same period. Continuous compaction of the sample resulted in significant accumulation of deformation. However, by the later part of the test, the two moduli converged, and the axial strain increased slowly until no more plastic strain was produced. At this point, only elastic strains were generated. This indicates that the equivalent modulus can be equated to the elastic modulus after the specimen reaches a steady state.

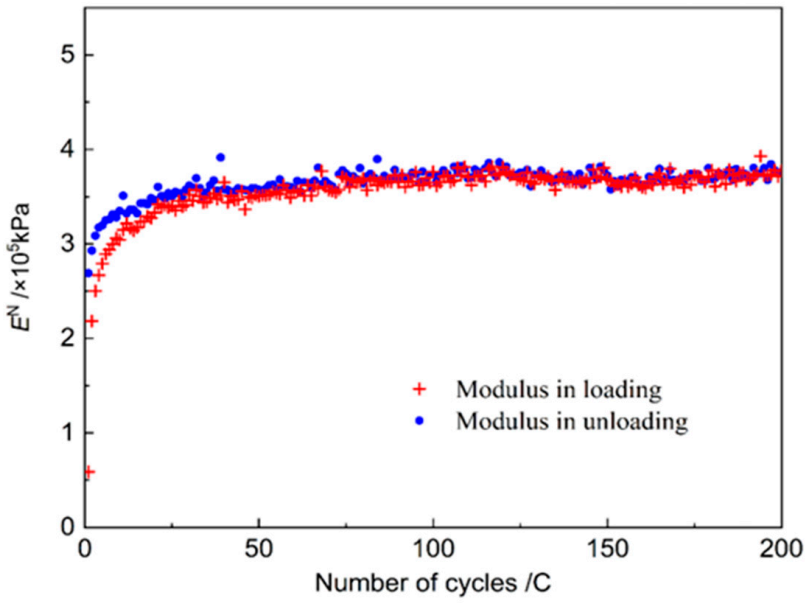

Figure 9. Relationship between equivalent loading and unloading moduli (SSC223).

In addition, it can be clearly seen that the equivalent modulus at the first loading is significantly smaller than the other moments, showing a completely different deformation characteristic. Thus, the first loading equivalent modulus was not considered when performing the fitting. The deformation during initial loading was easily obtained from the monotonic loading curve. In addition to the first loading, the loading and unloading equivalent moduli showed an approximate hyperbolic relationship with the number of cycles (see Equation (2)), which can be expressed in linear form through coordinate transformation (see Equation (3) and Figure 10). The double-curve fitting parameters for the cyclic loading tests under different test conditions are shown in Table 2, and the fit (R^2) was greater than 0.97 for both ISO sand and emery:

$$E^N = \frac{N}{k \cdot N + b} \tag{2}$$

$$\frac{N}{E^N} = k \cdot N + b \tag{3}$$

where N is the number of cycles corresponding to the loading (or unloading) equivalent modulus, and k and b are the fitting parameters of the hyperbolic relationship during loading (or unloading).

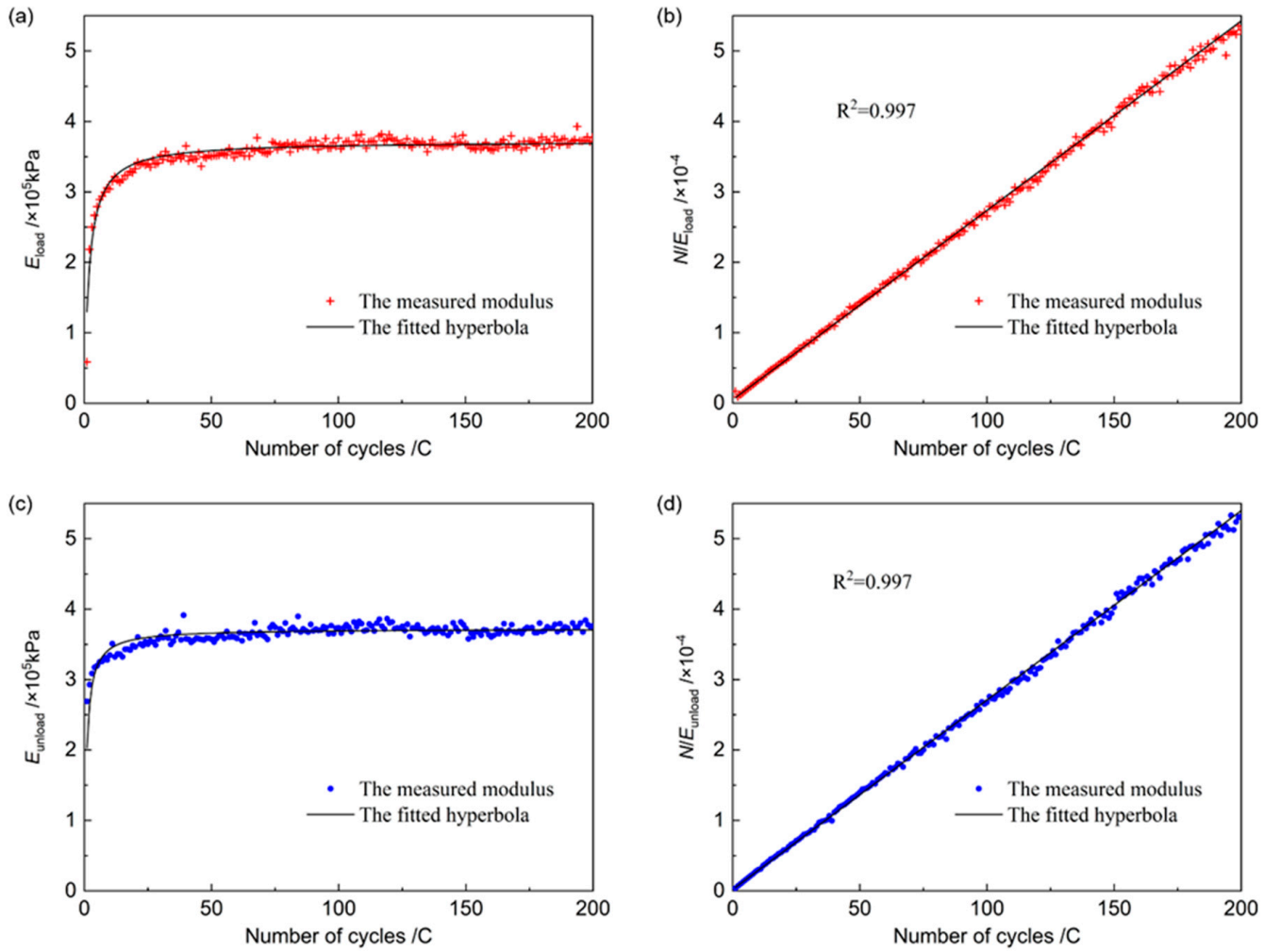

Figure 10. Hyperbolic model between equivalent modulus and number of cycles for SSC223: (**a**) load equivalent modulus fitting; (**b**) load transform coordinate system fitting; (**c**) unload equivalent modulus fitting; (**d**) unload transform coordinate system fitting.

Table 2. Fitting results of hyperbolic model.

Test Number	Loading Fitting Parameters			Unloading Fitting Parameters		
	k_{load}	b_{load}	R^2	k_{unload}	b_{unload}	R^2
SSC121	3.46×10^{-6}	4.85×10^{-6}	0.990	3.47×10^{-6}	1.69×10^{-6}	0.992
SSC211	4.76×10^{-6}	1.28×10^{-5}	0.999	4.76×10^{-6}	5.03×10^{-6}	0.999
SSC221	3.23×10^{-6}	3.76×10^{-6}	0.997	3.22×10^{-6}	1.51×10^{-6}	0.997
SSC222	3.05×10^{-6}	5.14×10^{-6}	0.998	3.04×10^{-6}	1.54×10^{-6}	0.998
SSC223	2.74×10^{-6}	1.99×10^{-6}	0.997	2.75×10^{-6}	8.58×10^{-7}	0.997
SSC231	2.38×10^{-6}	2.71×10^{-6}	0.996	2.38×10^{-6}	9.73×10^{-7}	0.996
SSC251	1.96×10^{-6}	9.14×10^{-7}	0.982	1.97×10^{-6}	4.12×10^{-7}	0.983
SSC321	2.96×10^{-6}	4.85×10^{-6}	0.998	2.95×10^{-6}	1.69×10^{-6}	0.998
SSC421	2.56×10^{-6}	3.00×10^{-6}	0.979	2.54×10^{-6}	9.79×10^{-7}	0.975
ESC121	2.33×10^{-6}	2.79×10^{-6}	0.999	2.31×10^{-6}	7.64×10^{-7}	0.998
ESC211	2.49×10^{-6}	1.24×10^{-5}	0.995	2.47×10^{-6}	1.47×10^{-6}	0.984
ESC221	2.10×10^{-6}	4.18×10^{-6}	0.995	2.09×10^{-6}	8.73×10^{-7}	0.995
ESC222	2.07×10^{-6}	4.79×10^{-6}	0.997	2.07×10^{-6}	8.85×10^{-7}	0.996
ESC223	1.92×10^{-6}	3.97×10^{-6}	0.997	1.92×10^{-6}	6.96×10^{-7}	0.997
ESC231	1.73×10^{-6}	2.90×10^{-6}	0.998	1.74×10^{-6}	7.10×10^{-7}	0.999
ESC251	1.47×10^{-6}	2.06×10^{-6}	0.996	1.47×10^{-6}	5.34×10^{-7}	0.996
ESC321	1.95×10^{-6}	3.60×10^{-6}	0.998	1.96×10^{-6}	9.19×10^{-7}	0.998
ESC421	1.72×10^{-6}	2.98×10^{-6}	0.995	1.72×10^{-6}	5.79×10^{-7}	0.994

4.2. Elastic and Plastic Modulus Separation

When employing the hyperbolic relationship to characterize the connection between the loading and unloading equivalent moduli and the number of cycles, different fitting parameters, i.e., k_{load}, b_{load}, k_{unload}, and b_{unload}, were used to distinguish between different materials and test conditions. Combined with the classical elastic–plastic theory, the physical significance of the above parameters can be clarified for the separation of elastic and plastic deformation.

In Equation (2), when the number of cycles N tends to infinity, the loading equivalent modulus $E_{load}^{N\to\infty}$ tends to a constant value $1/k_{load}$, i.e.,

$$E_{load}^{N\to\infty} = \left.\frac{N}{k_{load} \cdot N + b_{load}}\right|_{N\to\infty} = \frac{1}{k_{load}} \tag{4}$$

Similarly, the unloading equivalent modulus $E_{unload}^{N\to\infty}$ also tends to a constant value of $1/k_{unload}$, i.e.,

$$E_{unload}^{N\to\infty} = \left.\frac{N}{k_{unload} \cdot N + b_{unload}}\right|_{N\to\infty} = \frac{1}{k_{unload}} \tag{5}$$

Comparing the double-curve fitting parameters k_{load} and k_{unload} of each group of tests in Table 2, the absolute value of the relative error of both is less than 1.5%. The relative error distribution is shown in Figure 11. Considering the effect of test error, it can be assumed that the loading and unloading fitting parameter k is the same in the same group of tests, i.e.,

$$k_{load} = k_{unload} \tag{6}$$

Combining Equations (4)–(6), we have:

$$E_{load}^{N\to\infty} = E_{unload}^{N\to\infty} \tag{7}$$

Equation (7) shows that after an infinite number of cyclic loadings, the ultimate loading equivalent modulus and the ultimate unloading equivalent modulus of the specimen converge to the same value. By combining with the definition of equivalent modulus by Equation (1), it becomes apparent that the axial strain generated during the loading process of the specimen will be fully recovered in the unloading process, without any

residual strain. This is consistent with the experimental results of the previous analysis. The ultimate loading and unloading equivalent modulus is the elastic modulus E^{elastic} (see Equation (8)), indicating that the physical significance of the parameter k in the hyperbolic model is the inverse of the elastic modulus.

$$E^{\text{elastic}} = E_{\text{load}}^{N\to\infty} = E_{\text{unload}}^{N\to\infty} = \frac{1}{k_{\text{load}}} = \frac{1}{k_{\text{unload}}} \tag{8}$$

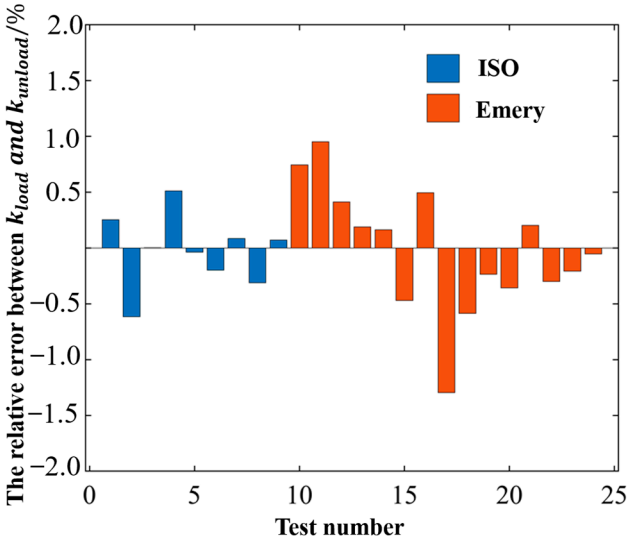

Figure 11. The relative error distribution of k.

The modulus of elasticity of a specimen reaching a steady state remains constant during cyclic loading, which has been demonstrated [20], so the following inferences can be made. According to Equations (3) and (8), it can be seen that in the Nth loading cycle, the equivalent moduli of loading and unloading can be expressed as Equations (9) and (10).

$$\frac{1}{E_{\text{load}}^{N}} = \frac{1}{E^{\text{elastic}}} + \frac{b_{\text{load}}}{N} \tag{9}$$

$$\frac{1}{E_{\text{unload}}^{N}} = \frac{1}{E^{\text{elastic}}} + \frac{b_{\text{unload}}}{N} \tag{10}$$

The classical theory of elasticity and plasticity assumes that the specimen produces both elastic and plastic strains under loading. Analyzing the strain increment loading in the Nth cycle, we have:

$$\Delta\varepsilon_{\text{load}}^{N} = \Delta\varepsilon_{\text{load}}^{\text{elastic}} + \Delta\varepsilon_{\text{load}}^{\text{plastic}} \tag{11}$$

where $\Delta\varepsilon_{\text{load}}^{N}$ load is the total strain generated in the Nth loading stage, and $\Delta\varepsilon_{\text{load}}^{\text{elastic}}$ and $\Delta\varepsilon_{\text{load}}^{\text{plastic}}$ are the elastic and plastic strain portions, respectively.

Since both elastic and plastic strains are generated under the same stress, the plastic modulus is defined in the same way as the equivalent modulus and the elastic modulus. See Equations (12) and (13).

$$E^{\text{elastic}} = \frac{\Delta q}{\Delta\varepsilon_{\text{load}}^{\text{elastic}}} \tag{12}$$

$$E_{\text{load}}^{\text{plastic}} = \frac{\Delta q}{\Delta\varepsilon_{\text{load}}^{\text{plastic}}} \tag{13}$$

where $E_{\text{load}}^{\text{plastic}}$ is the plastic equivalent modulus during the Nth loading.

Substitute Equations (12), (13), and (1) into Equation (11), and we have:

$$\frac{1}{E_{\text{load}}^{N}} = \frac{1}{E^{\text{elastic}}} + \frac{1}{E_{\text{load}}^{\text{plastic}}} \tag{14}$$

Similarly, Equation (15) describes how the unloading modulus can be obtained.

$$\frac{1}{E_{\text{unload}}^{N}} = \frac{1}{E^{\text{elastic}}} + \frac{1}{E_{\text{unload}}^{\text{plastic}}} \tag{15}$$

Comparing Equations (9), (10), (14), and (15), it can be seen that the physical significance of the hyperbolic model parameter b is N times the reciprocal of the Nth loading and unloading plastic equivalent modulus (see Equations (16) and (17)) which are not usually the same (see Table 2).

$$b_{\text{load}} = \frac{N}{E_{\text{load}}^{\text{plastic}}} \tag{16}$$

$$b_{\text{unload}} = \frac{N}{E_{\text{unload}}^{\text{plastic}}} \tag{17}$$

In summary, the physical meaning of the parameters in the hyperbolic model can be clarified. The elastic modulus is the inverse of the parameter k, and the plastic modulus for the Nth loading and unloading is the inverse of b times N. The elastic and plastic parts of the specimen deformation can be separated.

4.3. Preliminary Validation of Independent Data Sets

In order to verify the validity of the model, this paper utilized the data of Zeng et al. [6] to conduct a preliminary test of the model. The trial number selected for this paper was SP131. The model parameters were $k = 3.91 \times 10^{-6}$, $b_{\text{load}} = 5.96 \times 10^{-6}$; $b_{\text{unload}} = 4.42 \times 10^{-6}$. Comparison of modeled calculations with actual measured axial cumulative strains is shown in Figure 12.

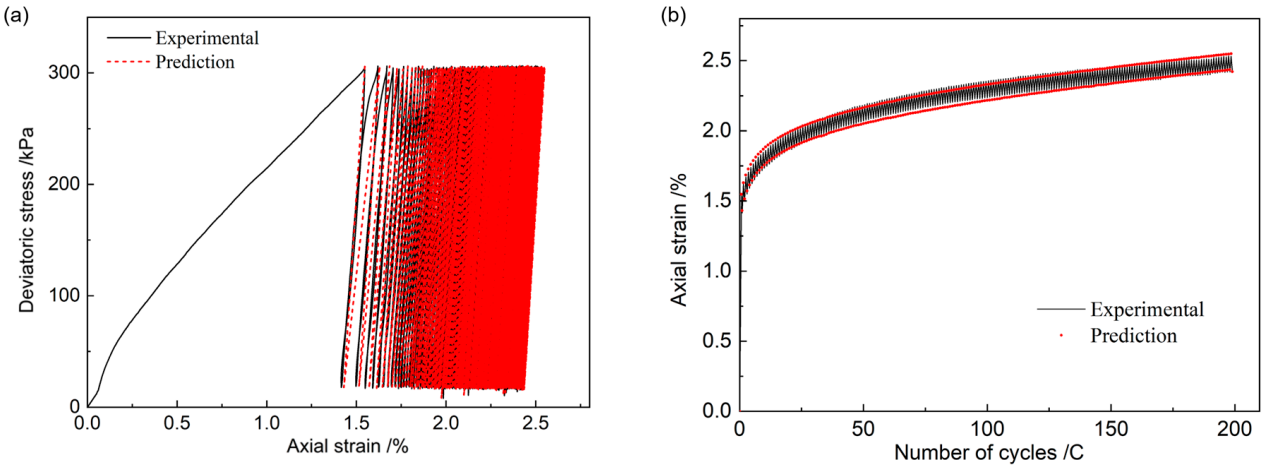

Figure 12. Actual measurements and model calculations: (**a**) stress–strain curve; (**b**) axial cumulative deformation.

4.4. Expression of the Modulus of Elasticity

Separation of elastic and plastic deformations based on the hyperbolic model can be used to obtain the elastic modulus and plastic modulus, respectively, which is beneficial for establishing an elastic–plastic constitutive model. From the above analysis, we can obtain Equation (8) for the elastic modulus at a steady state. By subtracting the elastic strain from the total strain, we can derive the plastic deformation; thus, in this paper, we only present

the formulation for the elastic modulus. The void ratio, confining pressure, and deviatoric stress amplitude were employed as control variables in the test.

After the specimen entered the elastic state, the increase in stress further increased the degree of densification, thus affecting the modulus of elasticity. Figure 13 shows the dependence of the elastic modulus on bias stress amplitude for ISO and emery under the same confining pressure. Figure 14 shows the dependence of the elastic modulus on confining pressure for the same magnitude of bias stress. The results show that the elastic modulus of the specimen increased linearly with increasing axial stress, but the increase in elastic modulus due to increased confining pressure was more rapid. Soil samples being an aggregate of loose particles, the confining pressure played an important role in maintaining the compactness between the soil particles and hence had a greater effect on the modulus of elasticity. This phenomenon was also found in the studies of Monismit [35] and Hick et al. [36].

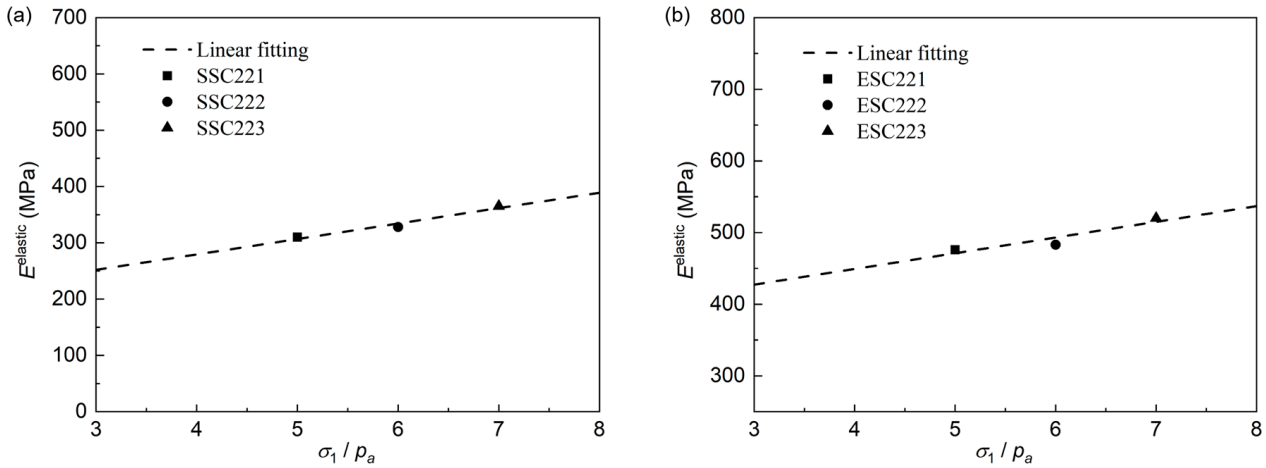

Figure 13. Relationship between elastic modulus and normalized axial stress: (**a**) ISO; (**b**) emery.

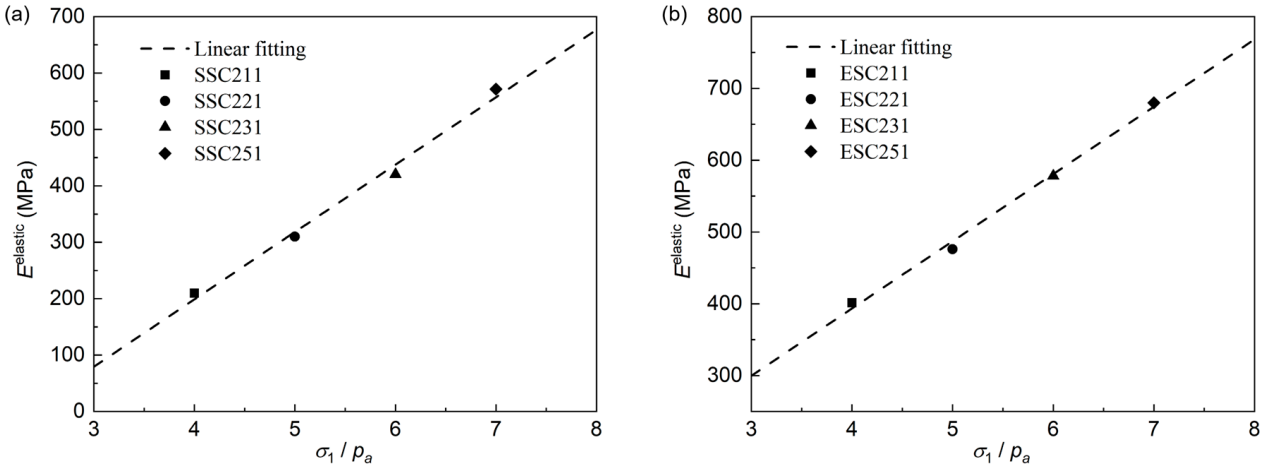

Figure 14. Relationship between elastic modulus and normalized axial stress: (**a**) ISO; (**b**) emery.

Considering the combined effects of axial stress and confining pressures, the dependence of the elastic modulus on the stress state can be directly characterized by the average principal stress p. The variation in the elastic modulus with respect to p/p_a is illustrated in Figure 15. In Figure 15, it is evident that the elastic modulus increases gradually with the increase in the average principal stress.

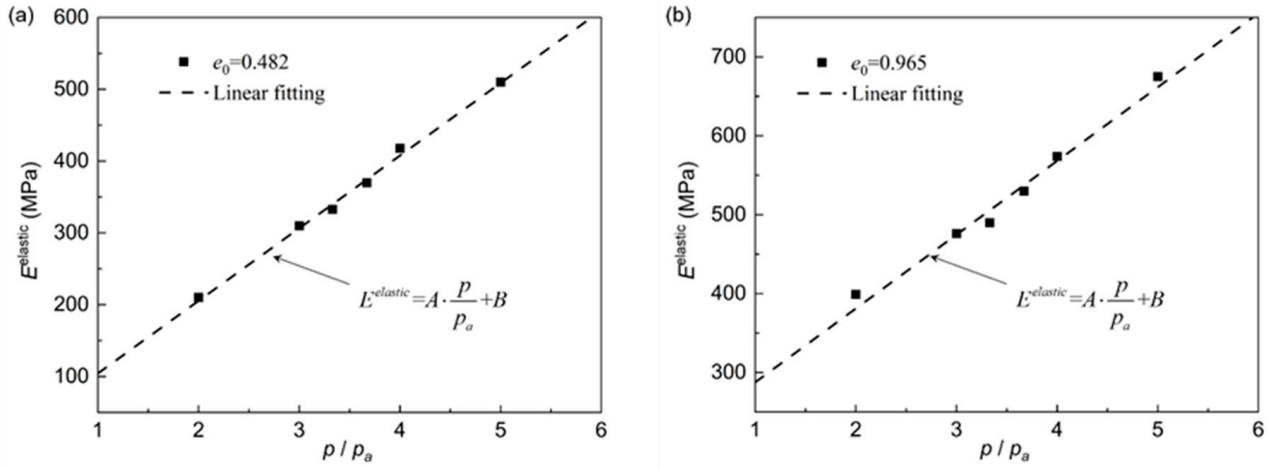

Figure 15. Relationship between elastic modulus and p/p_a: (**a**) ISO; (**b**) emery.

The fitting relationship can be expressed by Equation (18):

$$E^{\text{elastic}} = A \cdot \frac{p}{p_a} + B \tag{18}$$

where A and B are the fitting parameters and p_a is the standard atmospheric pressure.

In addition to the stress state, this study also considered the effect of the void ratio on the elastic modulus. The relationship between the elastic modulus and the void ratio is illustrated in Figure 16. The results indicated that the elastic modulus of the specimen increased gradually from the loose state to the dense state. During the testing process, the internal pore structure of the soil sample was continuously damaged while the compactness was constantly increased. After undergoing an infinite number of cycles to achieve the ideal elastic state, soil samples with different void ratios reached the maximum compactness at that specific density. the void ratio function utilized in this study is that proposed by Hardin et al. [37].

$$f(e) = \frac{(2.17-e)^2}{1+e} \tag{19}$$

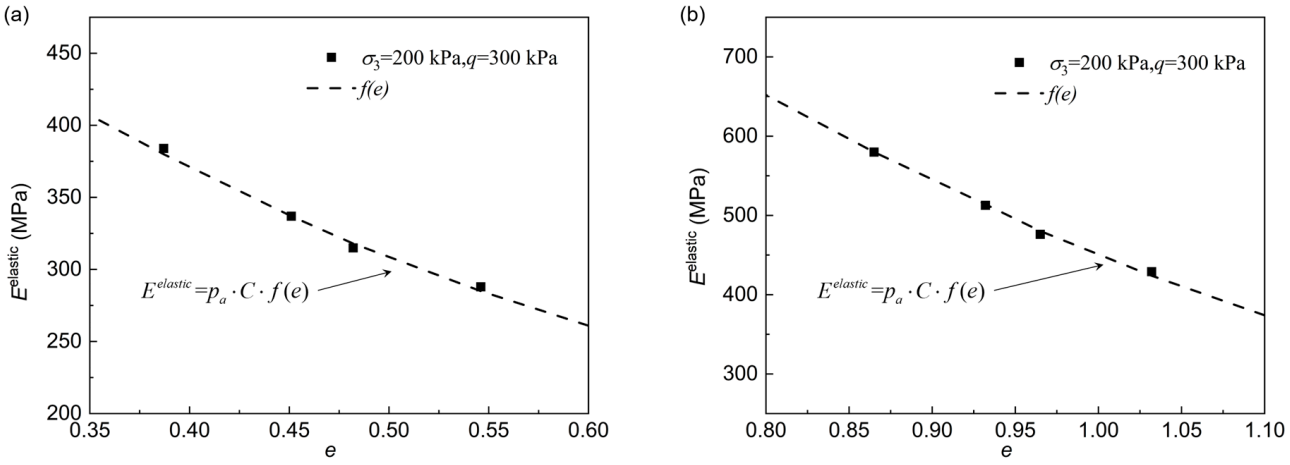

Figure 16. Relationship between elastic modulus and e: (**a**) ISO; (**b**) emery.

Numerous test results have demonstrated its broad applicability to cohesionless soils [38,39]. The fitting relationship can be expressed by Equation (20). Figure 16 shows the strong applicability of this empirical formula to the sand selected for this study:

$$E^{\text{elastic}} = p_a \cdot C \cdot f(e) \tag{20}$$

where C is the fitting parameter.

In summary, both the stress state and the void ratio influenced the elastic modulus of the specimen. Consideration of these two effects in combination yields an empirical model for the total elastic modulus:

$$E^{\text{elastic}} = p_a \cdot f(e) \cdot (m \cdot \frac{p}{p_a} + n) \tag{21}$$

where m and n are the new fitting parameters.

5. Conclusions

In this study, a series of triaxial cyclic loading tests was conducted on two typical sands. Utilizing the full-surface-deformation measurement system, the overall deformation behavior of the soil samples was analyzed. A hyperbolic model describing the relationship between the equivalent modulus during loading/unloading and the number of cycles was presented, along with the specific physical meanings of the model parameters. According to the hyperbolic model, the elastic strain was able to be differentiated from the total strain. Through comparative testing, the effects of void ratio, confining pressure, and deviatoric stress amplitude on the elastic modulus were analyzed, leading to the following summarized conclusions.

(1) Under constant cyclic loading, the soil sample gradually tended to deform to a steady state as the test proceeded. In the steady state, the deformation of the specimen was fully recoverable and the sandy soil exhibited elastic properties.
(2) Both loading and unloading equivalent moduli exhibited highly correlated hyperbolic relationships with the number of cycles. The parameter k represents the reciprocals of the elastic modulus, and b represents the plastic modulus multiplied by the Nth cycle. The elastic modulus remained constant throughout all stages of the test, allowing for the separation of the elastic and plastic components of the total strain. This facilitated the establishment of the elastic and plastic constitutive relationship, the analysis of the evolution of elastic–plastic deformation, and a more intuitive reflection of the cyclic hardening behavior of the soil.
(3) The effect of axial stress on the modulus of elasticity was smaller than confining pressure. Considering the combined effects of axial and confining pressures, the stress state of the specimen can be represented by the average principal stress p, with the elastic modulus increasing linearly relative to p. Besides the stress state, the void ratio also had an effect on the elastic modulus.

The research in this paper contributes to further understanding of the elastic–plastic deformation law of sand. The hyperbolic model on the one hand clarifies the elastic deformation part of the cyclic loading process and facilitates the targeted establishment of elastic and plastic constitutive relationships, and on the other hand, it can be used to calculate the loading and unloading strain increment of sandy soils in cyclic loading to analyze the elastic–plastic deformation evolution. However, more and different types of test data are also necessary to validate the applicability of the method. More influencing factors as well as consideration of the stress state will also be the focus of future work.

Author Contributions: Data curation, X.W. and X.T.; formal analysis, X.W. and X.T.; investigation, X.W. and X.T.; methodology, X.W. and L.S.; project administration, L.S.; resources, L.S.; supervision, L.S.; writing—original draft, X.W., X.T., and P.X.; writing—review and editing, X.W. and P.X. All authors have read and agreed to the published version of the manuscript.

Funding: This research was funded by the National Natural Science Foundation of China (Grant No. 52079018).

Data Availability Statement: The test data used to support the findings of this study are available from the corresponding author upon reasonable request.

Conflicts of Interest: Author Xiaojian Tian was employed by the State Key Laboratory of Intelligent Mining Equipment Technology, Taiyuan Heavy Industry Co., Ltd. The remaining authors declare that the research was conducted in the absence of any commercial or financial relationships that could be construed as a potential conflict of interest.

References

1. Zhao, C.; Liu, J.M.; Liu, H.M.; Bian, X.C.; Chen, Y.M. A conceptual model for the shakedown response of soft clay to high-cycle, low-amplitude undrained loading. *Comput. Geotech.* **2023**, *156*, 105257. [CrossRef]
2. Zhao, Z.Y.; Deng, G.; Han, Y.S.; Zhang, Z.P.; Dong, Y.L.; Gao, Y. Comparison of Deformation Behavior of Saturated Sand under Constant and Variable Deviatoric Stress. *KSCE J. Civ. Eng.* **2020**, *24*, 762–769. [CrossRef]
3. Zheng, D.H.; Tang, L.S.; Wang, Y.X.; Sun, Y.L. Dynamic stress accumulation effects on soil strength under cyclic loading. *Soils Found.* **2022**, *62*, 101164. [CrossRef]
4. Sun, Q.; Dong, Q.Y.; Cai, Y.Q.; Wang, J. Modeling permanent strains of granular soil under cyclic loading with variable confining pressure. *Acta Geotech.* **2020**, *15*, 1409–1421. [CrossRef]
5. Jitsangiam, P.; Pra-ai, S.; Boulon, M.; Jenck, O.; Chen, X.B.; Techavorasinsakul, S. Characterization of a soil-rough structure interface using direct shear tests with varying cyclic amplitude and loading sequences under a large cyclic testing cycle condition. *Acta Geotech.* **2022**, *17*, 1829–1845. [CrossRef]
6. Zeng, F.T.; Shao, L.T. Unloading Elastic Behavior of Sand in Cyclic Triaxial Tests. *Geotech. Test. J.* **2016**, *39*, 462–475. [CrossRef]
7. Xia, P.X.; Zeng, C.; Shao, L.T.; Zhang, X. Axial strain accumulation projection model for sand in cyclic loading. *Soil Dyn. Earthq. Eng.* **2021**, *147*, 106819. [CrossRef]
8. Xia, P.X.; Zeng, C.; Shao, L.T.; Zhang, X.; Guo, X.X. Axial Component of Plastic Modulus of Sand Under Slow Periodic Load. *J. GeoEng.* **2021**, *16*, 47–59. [CrossRef]
9. Yin, Z.Y.; Xu, Q.; Hicher, P.Y. A simple critical-state-based double-yield-surface model for clay behavior under complex loading. *Acta Geotech.* **2013**, *8*, 509–523. [CrossRef]
10. Dafalias, Y.F.; Popov, E.P. A model of nonlinearly hardening materials for complex loading. *Acta Mech.* **1975**, *21*, 173–192. [CrossRef]
11. Chowdhury, E.Q.; Nakai, T.; Tawada, M.; Yamada, S. A model for clay using modified stress under various loading conditions with the application of subloading concept. *Soils Found.* **1999**, *39*, 103–116. [CrossRef] [PubMed]
12. Heidarzadeh, H.; Oliaei, M.; Komakpanah, A. A developed constitutive model for sand and clay under monotonic and cyclic loadings. *Int. J. Geomech.* **2023**, *23*, 04023133. [CrossRef]
13. Lashkari, A.; Golchin, A. On the influence of elastic–plastic coupling on sands response. *Comput. Geotech.* **2014**, *55*, 352–364. [CrossRef]
14. Gajo, A.; Wood, D.M.; Bigoni, D. On certain critical material and testing characteristics affecting shear band development in sand. *Geotechnique* **2007**, *57*, 449–461. [CrossRef]
15. Xia, P.X.; Shao, L.T.; Deng, W.; Zeng, C. Evolution prediction of hysteresis behavior of sand under cyclic loading. *Processes* **2022**, *10*, 879. [CrossRef]
16. Pradhan, T.B.; Tatsuoka, F.; Sato, Y. Experimental stress-dilatancy relations of sand subjected to cyclic loading. *Soils Found.* **1989**, *29*, 45–64. [CrossRef]
17. Karg, C.; Haegeman, W. Elasto-plastic long-term behavior of granular soils: Experimental investigation. *Soil Dyn. Earthq. Eng.* **2009**, *29*, 155–172. [CrossRef]
18. Hardin, B.O.; Blandford, G.E. Elasticity of Particulate Materials. *J. Geotech. Eng.* **1989**, *115*, 788–805. [CrossRef]
19. Sawicki, A.; Świdziński, W. Elastic moduli of non-cohesive particulate materials. *Powder Technol.* **1998**, *96*, 24–32. [CrossRef]
20. Xia, P.X.; Shao, L.T.; Deng, W. Mechanism study of the evolution of quasi-elasticity of granular soil during cyclic loading. *Granul. Matter.* **2021**, *23*, 84. [CrossRef]
21. Mróz, Z.; Norris, V.A.; Zienkiewicz, O.C. Application of an anisotropic hardening model in the analysis of elasto–plastic deformation of soils. *Géotechnique* **1979**, *29*, 1–34. [CrossRef]
22. Prévost, J.H. Plasticity theory for soil stress-strain behavior. *J. Eng. Mech. Div.* **1978**, *104*, 1177–1194. [CrossRef]
23. Mróz, Z.; Norris, V.A.; Zienkiewicz, O.C. An anisotropic hardening model for soils and its application to cyclic loading. *Int. J. Numer. Anal. Methods Geomech.* **1978**, *2*, 203–221. [CrossRef]
24. Mróz, Z.; Norris, V.A.; Zienkiewicz, O.C. An anisotropic, critical state model for soils subject to cyclic loading. *Géotechnique* **1981**, *31*, 451–469. [CrossRef]
25. Manzari, M.T.; Dafalias, Y.F. A critical state two-surface plasticity model for sands. *Geotechnique* **1997**, *47*, 255–272. [CrossRef]
26. Dafalias, Y.F.; Herrmann, L.R. Bounding surface plasticity. II: Application to isotropic cohesive soils. *J. Eng. Mech.* **1986**, *112*, 1263–1291. [CrossRef]
27. Zienkiewicz, O.C.; Mroz, Z. Generalized plasticity formulation and applications to geomechanics. *Mech. Eng. Mater.* **1984**, *44*, 655–680.
28. Pastor, M.; Zienkiewicz, O.C.; Chan AH, C. Generalized plasticity and the modelling of soil behaviour. *Int. J. Numer. Anal. Methods Geomech.* **1990**, *14*, 151–190. [CrossRef]

29. Heidarzadeh, H.; Oliaei, M. Development of a generalized model using a new plastic modulus based on bounding surface plasticity. *Acta Geotech.* **2018**, *13*, 925–941. [CrossRef]
30. Dong, J.J.; Shao, L.T.; Zeng, F.T. Experimental study on deformation properties of unsaturated compacted soil based on digital image measurement. *Eng. Rev.* **2014**, *34*, 217–222.
31. Shao, L.T.; Liu, G.; Zeng, F.T.; Guo, X.X. Recognition of the stress-strain curve based on the local deformation measurement of soil specimens in the triaxial test. *Geotech. Test. J.* **2016**, *39*, 658–672. [CrossRef]
32. Xiong, H.; Cai, Y.Q.; Yang, Z.X.; Chai, J.C. Effect of drained static shear on cyclic deformation behavior of K0-consolidated sand. *Soils Found.* **2017**, *57*, 720–732. [CrossRef]
33. Tong, Z.X.; Zhang, J.M.; Yu, Y.L.; Zhang, G. Drained Deformation Behavior of Anisotropic Sands during Cyclic Rotation of Principal Stress Axes. *J. Geotech. Geoenviron. Eng.* **2010**, *136*, 1509–1518. [CrossRef]
34. Bouckovalas, G.; Whitman, R.V.; Marr, W.A. Permanent displacement of sand with cyclic loading. *J. Geotech. Eng.* **1984**, *110*, 1606–1623. [CrossRef]
35. Monismith, C.L.; Ogawa, N.; Freeme, C.R. Permanent deformation characteristics of subgrade soils due to repeated loading. *Transp. Res. Rec.* **1975**, 537. Available online: https://onlinepubs.trb.org/Onlinepubs/trr/1975/537/537-001.pdf (accessed on 22 October 2024).
36. Hicks, R.G.; Monismith, C.L. Factors influencing the resilient response of granular materials. *Hwy. Res. Rec.* **1971**, *345*, 15–31.
37. Hardin, B.O.; Richart, F.E. Elastic wave velocities in granular soils. *J. Soil Mech. Found. Div.* **1963**, *89*, 33–65. [CrossRef]
38. Kohata, Y.; Tatsuoka, F.; Wang, L.; Jiang, G.L.; Hoque, E.; Kodakai, T. Modelling the non-linear deformation properties of stiff geomaterials. *Geotechnique* **1997**, *47*, 563–580. [CrossRef]
39. AnhDan, L.Q.; Koseki, J. Effects of large number of cyclic loading on deformation characteristics of dense granular materials. *Soils Found.* **2004**, *44*, 115–123. [CrossRef]